Monthly Notices
of the
ROYAL ASTRONOMICAL SOCIETY

MNRAS **439,** 1313–1325 (2014)
Advance Access publication 2014 February 10

doi:10.1093/mnras/stt2462

A detailed numerical analysis of asymmetrical density distribution in Saturn's F ring during an encounter with Prometheus

Phil J. Sutton★ and Feo V. Kusmartsev

Astronomy Unit, Physics department, Loughborough University, Loughborough, Leicestershire LE11 3TU, UK

Accepted 2013 December 19. Received 2013 December 9; in original form 2013 August 13

ABSTRACT

Saturn's rings, reminiscent of an early Solar system present a unique opportunity to investigate experimentally some mechanisms thought to be responsible for planet and planetesimal formation in protoplanetary discs. Here, we extended the comparison of our numerical models of Prometheus encountering the F ring employing non-interacting and interacting particles. Higher resolution analysis revealed that the density increases known to exist at channel edges is more complex and localized than previously thought. Asymmetry between density increases on channel edges revealed that the channel edge facing way from Prometheus to be the most stable but with lowest maximum increases. However, on the channel edge facing Prometheus the interacting model showed large chaotic fluctuations in the maximum density of some clumps, much larger than those of the other channel. The likely cause of this asymmetry is a variance in localized turbulence introduced into the F ring by Prometheus. High-resolution velocity dispersion maps showed that there was a spatial link between the highest densities and the highest velocity dispersions in the interacting model. Thus, suggesting that the high velocity dispersion we see is the reason for the observed inhomogeneous distribution of fans (evidence of embedded moonlets) on some of the channel edges facing Prometheus.

Key words: gravitation – planets and satellites: formation – planets and satellites: rings – protoplanetary discs.

1 INTRODUCTION

Saturn's F ring, a unique place in the Solar system, has been the subject of intense studies due to the diverse dynamics witnessed by the *CASSINI* spacecraft over short time frames. The dusty F ring takes on a knotted asymmetrical structure where most of its mass is assumed to be in its central core. Low-density spiral strands have been observed to reside on either side of the core, their formation arises from the long-term evolution of jets by physical collisions of small moonlets on eccentric orbits through the central core (Charnoz et al. 2005; Murray et al. 2008). The central core is known to be home to a large population of resident small moonlets from stellar occultations (Esposito et al. 2008; Hedman et al. 2011; Meinke, Esposito & Sremčević 2011; Meinke et al. 2012), the presence of mini jets (Attree et al. 2012, 2013) and fan structures emanating out from the core (Beurle et al. 2010). Interactions between Prometheus, the F ring inner Shepherd moon, and the F ring is thought to be well understood with many of the features, structures and the large population of transient moonlets directly attributed to Prometheus (Murray et al. 2005; Murray et al. 2008; Beurle et al. 2010; Sutton & Kusmartsev 2013). However, large amounts of small moonlets responsible for creating mini jets in the central core appear to have no direct link to Prometheus in their position (Attree et al. 2013), raising more questions about their origin.

1.1 Moonlet formation

Some elements of moonlet formation in the F ring were found to be directly linked to the perturbations of Prometheus, with fans, the structural signatures of moonlets spaced at the same 3°.27 as Prometheus-induced structures in *CASSINI* images (Beurle et al. 2010). A numerical study assuming collisionless non-interacting particles within periodic boundary conditions was used to simulate the local effects of density fluctuations on a near homogeneous ring post-Prometheus encounter. It was discovered that density increased at channel edges up to a maximum of 2.5 times the original density, with large fluctuations in the maximum number density (max. no. density) of particles occurring over one orbital period. These large variations in local density can be seen to relate inversely to the magnitude of the minimum radial velocity. This then revealed that max. no. densities occurred when the lowest minimum radial velocities were seen. A clear link to moonlet formation and Prometheus in the F ring was provided but left open a window for more detailed investigations into the density evolution during an encounter with Prometheus, which is where our model seeks to expand.

★ E-mail: p.j.sutton@lboro.ac.uk

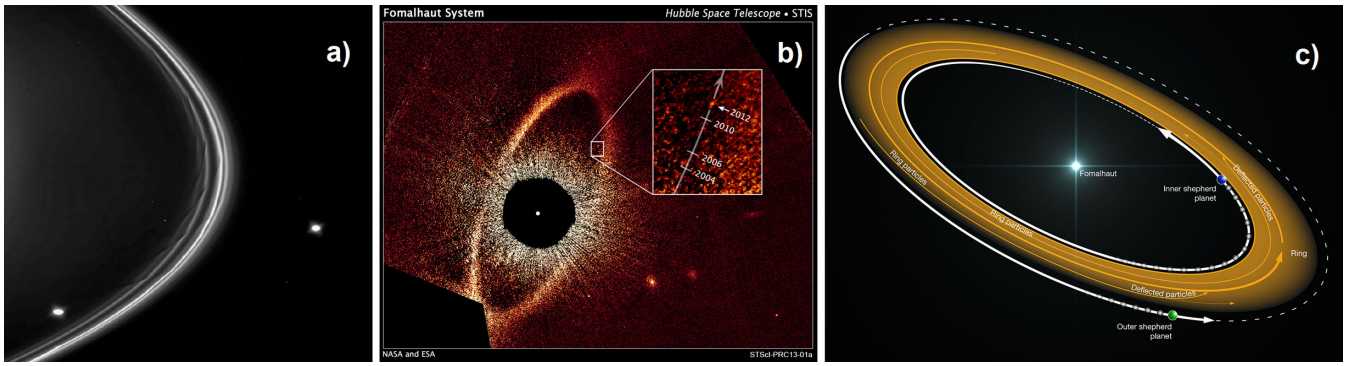

Figure 1. (a) An image taken by *CASSINI* of Saturn's F ring, shepherded by its two moons Prometheus (inner) and Pandora (outer), (b) image taken by the *Hubble Space Telescope* showing the debris disc around Fomalhaut with the zoomed in section illustrating the movement of the inner shepherding planet (Fomalhaut b) over the course of 8 years and (c) a visual representation of the Fomalhaut system depicting the two shepherding planets that could be responsible for the narrow ring, similar to Saturn's F ring. Image credit: ALMA (European Southern Observatory/National Astronomical Observatory of Japan (NAOJ)/National Radio Astronomy Observatory (NRAO))/B. Saxton. All of the images are orientated to show an anticlockwise orbital direction.

A predator–prey model was proposed by Esposito et al. (2012) for the edge of B ring and the F ring. Here, aggregate size was seen as the prey and the perturbing moons as the predator. It was shown that Prometheus has an influence on clump formation in the F ring with Mimas displaying a comparable dominant effect on the outer B ring edge. Locations of moonlets or clumps were seen to be at resonances in the rings with the predator moons. Large increases in velocity dispersion were seen to decrease the local density with disaggregation developing from disruptive collisions or tidal shear. However, agitation of ring material at the ring edge through stochastic processes can yield the increase of density of clumps into more persistent objects within the ring, again forming a link to possible moonlet formation and the perturbing moon.

Another mechanism was suggested for moon and moonlet formation by viscous spreading to explain the current configuration of Saturn's moons and moonlets (Charnoz, Salmon & Crida 2010). Here, the main moons and moonlets both showed a linear increase in mass with distances from Saturn but with distinctly different gradients. The differences, when elaborated, established the moonlet group to exhibit a larger mass enhancement with increasing distances from Saturn in comparison to the main moons. Moonlets growth at the rings edge is attributable to positive induced torque from the rings and the planet driving their outward migration. As the torque (Γ_s) increases with the moon mass (m_s)$\Gamma_s \propto m_s^2$, the migration rate also increases, driving the faster outward migration of more massive moons. Due to the different migration rates, orbital crossings and merging can occur which leads to the arrangement of moons radially aligned as a function of their mass. This mechanism can therefore explain the existence of dynamically young moons so close to the rings.

1.2 Structures from embedded moonlets

Propeller-shaped structures, the signature of small radially stationary embedded moonlets a few hundred metres in size, have been observed in Saturn's rings by *CASSINI* (Tiscareno et al. 2006, 2008; Srem evi et al. 2007). Previous numerical work used different methods to our model where physical collisions, particles sizes and periodic boundary conditions were all implicit in their calculations (Lewis & Stewart 2009). Here, in the A ring, where particle sizes and surface densities are at the highest, physical collisions produce a relative dampening effect on structures created by moon/moonlet interactions. This case is shown in greater detail where propeller-shaped structures formed by stationary moonlets in the rings were investigated. When non-interacting test particles were used, a repeating pattern of the particles trajectories with aperiodicity of $3\pi\Delta\alpha$ where $\Delta\alpha$ is the orbit separation was seen. However, when collisions and self-gravity were taken into account, a damping effect was seen where eccentricities were reduced and orbits randomized beyond the initial structure. It is likely that physical collisions would have a similar effect on other types of structure created by embedded moonlets or perturbing moons. Consequently, in rings that have smaller particles sizes, F, G and E rings, and much lower surface densities, physical collisions would have a less dominant outcome in the evolution of moonlet-induced structures. Instead interparticle dynamics are dominated by gravitational forces.

1.3 Shepherded debris discs

Saturn's rings role as a local laboratory to study processes and evolution of larger scale astrophysical discs is an important one, and the most dynamic of them all, the F ring, could prove to be very useful in the study of narrow shepherded debris discs. For example, the Fomalhaut system is a narrow debris disc orbiting its host star; reminiscent of Saturn's F ring, it owes its narrow structure to two theorized shepherding planets (Boley et al. 2012). Fig. 1 shows a comparison of the two systems. The sharply truncated inner edge of the ring and eccentricity are good indicators of an internal shepherding planet that could be responsible for shaping it in the same way Prometheus dominates the sculpture of Saturn's F ring. It is still in debate whether Fomalhaut b is responsible for the inner shepherding of the disc or a pair of currently unseen shepherding planets is the cause of the narrow structure. However, recent work by Atacama Large Millimeter/Submillimeter Array (ALMA; 350 GHz) failed to observe any shepherding planets suggesting a much smaller size for the ring creators than previously thought (Boley et al. 2012). Evidence that the possible cause of the rings morphology is the existence of two small shepherding planets was still supported. Again constraining the idea that it could resemble a similar setup to Saturn's F ring where small moons shepherd but do not destroy the F ring. Using values taken from numerical studies by Chiang et al. (2009), it is possible to make assumptions that the inner planet could experience close encounters with the debris disc similar to Prometheus. For this, we need to assume that both the disc and inner shepherd planet are on elliptical orbits (0.11 and 0.12 eccentricities, respectively) and that

there is some degree of mutual precession of their orbits due to a non-spherical host star. If this is the case, its appearance can be assumed to be similar to the F ring. With semimajor axis of 115 au for the inner planet and 133–158 au for the disc at anti-alignment and closest approach, we would see the inner planet at apoapsis and the disc at periapsis. This would be at a radial distance from Fomalhaut of 128.8 au for the inner planet and 118.37–140.62 au for the disc. This would lead to a very big disturbance of the disc due to the planet. However, the rate of precession or any more details about the likely precession are difficult to calculate due to the uncertainty of the Fomalhaut system.

Future observations of the Fomalhaut debris disc with the proposed Exoplanet Imaging Camera and Spectrograph (EPICS) detector on the EELT could help give higher resolution investigations of the disc. The science goals of the EPICS detector are of a resolution of 0.005 arcsec with a field of view 1.37 arcsec × 1.37 arcsec (Kasper et al. 2008). Assuming these and applying it to the Fomalhaut debris disc in question, we can approximate that the field of view would cover approximately 30 × 30 au. If we make another assumption that any structure formed by an inner shepherding planet would be separated by the same as Prometheus-induced structures in the F ring, then there will be a spacing of approximately 7 au between areas of high and low density or surface brightness. This is well within the reach of the EPICS detector, although will not be anywhere near the same resolution as *CASSINI* can currently achieve. It should still be able to detect any asymmetry created by closely interacting shepherding planets. It is likely that the larger separation and eccentricities between disc and planet compared with the F ring and Prometheus would lead to a larger difference in orbital periods and thus a larger separation in structures. A separation of ∼10–20 times that of streamer channels in the F ring is possible, which again should be within the reach of the EPICS resolution.

2 NUMERICAL METHOD

To obtain the results reported in our manuscript, we employed an *N*-body simulation of 6.5×10^6 point-like particles where they evolved in the system due to gravitational forces taken from classical Newtonian mechanics only (Springel 2005). Particle surface densities of a maximum of 0.17 per km^2 are similar in value to previous numerical studies of the F ring (Murray et al. 2005; Chavez 2009). Particle collisions in their models showed that very few ring particles collided with Prometheus, ruling out physical collisions as the cause of the streamer channels. Thus, neglecting physical collisions in our models has negligible effect on the initial Prometheus encounter. Equations of motion for each particle as well as for Prometheus and Saturn can be shown as

$$\ddot{\boldsymbol{r}}_s = -G\sum_{i=1}^{N}(\boldsymbol{r}_i - \boldsymbol{r}_s)\frac{M_i}{|\boldsymbol{r}_i - \boldsymbol{r}_s|^3} - G(\boldsymbol{r}_p - \boldsymbol{r}_s)\frac{M_p}{|\boldsymbol{r}_p - \boldsymbol{r}_s|^3} \quad (1)$$

$$\ddot{\boldsymbol{r}}_p = -G\sum_{i=1}^{N}(\boldsymbol{r}_i - \boldsymbol{r}_p)\frac{M_i}{|\boldsymbol{r}_i - \boldsymbol{r}_p|^3} - G(\boldsymbol{r}_s - \boldsymbol{r}_p)\frac{M_s}{|\boldsymbol{r}_s - \boldsymbol{r}_p|^3} \quad (2)$$

$$\ddot{\boldsymbol{r}}_i = G\sum_{j\neq 1}^{N}(\boldsymbol{r}_i - \boldsymbol{r}_j)\frac{M_j}{|\boldsymbol{r}_i - \boldsymbol{r}_j|^3} - G(\boldsymbol{r}_p - \boldsymbol{r}_i)\frac{M_p}{|\boldsymbol{r}_p - \boldsymbol{r}_i|^3} - G(\boldsymbol{r}_s - \boldsymbol{r}_i)\frac{M_s}{|\boldsymbol{r}_s - \boldsymbol{r}_i|^3}, \quad (3)$$

where all of the vectors in the above equations are taken from Saturn also located at the origin. Prometheus was assumed to be at the periapsis of its orbit at the start. Two separate numerical models were created where the only difference was the mass of the ring particles. The first model assumed all ring particles to be massless test particles moving only under the influence of Saturn and Prometheus. The second model assumed a single ring particle mass of 10 kg whose motion is influenced not only by Saturn and Prometheus but also every other particle in the F ring. In the case of this manuscript, both models were allowed to evolve for a longer period of time than previously where the initial encounter of Prometheus was investigated (Sutton & Kusmartsev 2013).

An integration method was used to reduce the overall computation time down significantly by using a TreePM code parallelized across multiple processing cores by means of Peano–Hilbert domain decomposition. To reduce the overall number of force calculations, close-range forces were computed using a Barnes–Hut Tree code, whilst long-range forces used a PM (particle mesh) method, where the particles involved in long-range-force calculations were grouped together with other nearby particles in a clouds-in-cells approach with the forces calculated using an Fast Fourier Transform (FFT) technique (Springel 2005). In the TreePM method, a discretized particle system is mapped into continuous model with the peculiar potential defied as

$$\phi(x) = \Sigma m_i \phi(x - x_i), \quad (4)$$

where $\phi(x - x_i)$, a single-particle gravitational potential, is used to get gravitational forces in the equation of motion above, in equations (1)– (3). Then, this potential, equation (4), is split in Fourier space into a long-range and short-range part according to $\phi_k = \phi_k^{\rm long} + \phi_k^{\rm short}$, where

$$\phi_k^{\rm long} + \phi_k \exp(-k^2 r^2) \quad (5)$$

$$\phi_k^{\rm short} = -G\sum_{r_i}^{m_i} \operatorname{erfc}\left(\frac{r^i}{2r_s}\right), \quad (6)$$

where r_s is the spatial scale of the force split,

Adaptive time stepping was also used for all particles where time steps of particles were integer values of one another. This reduced down the overall forces computed, with particle time steps derived based upon its acceleration and assigned smoothing length (Springel 2005). The time step of each particle can then be shown as

$$\Delta T_{\rm grav} = \min\left[\Delta t_{\rm max}, \left(\frac{2\eta\varepsilon}{|\alpha|}\right)^{1/2}\right], \quad (7)$$

where $\Delta t_{\rm max}$ is the maximum allowed time step,
α is the acceleration of the particle,
η is the accuracy parameter and
ε is the smoothing length of the particle.

No hydrodynamical forces were included within the calculations, only gravitational forces. We also did not include direct physical collisions between particles; instead two particles interacting have a reduced (or smoothing) gravitational force once the distance between them became smaller than some characteristic smooth length common for all ring particles. Saturn and Prometheus have different, larger smoothing lengths, associated with their masses. In contrast to protoplanetary discs, pressure is not critical when considering Saturn's rings, and therefore, the approximation of gravitational forces only is well suited for this case. Spatial boundaries on the system have not been defined and so the system was open, with particles allowed to evolve in free space. This is hoped to reduce any errors that could be introduced as a result of using a shearing

box approximation on the F ring and periodic, quasi-periodic and chaotic structures formed by Prometheus.

2.1 Saturn's F ring

The starting position of particles was derived from parameters previously used for numerical modelling of the F ring (Murray et al. 2005; Beurle et al. 2010; Sutton & Kusmartsev 2013), strands and the central core. To create a more realistic F ring structure, all ring particles were arranged randomly into four groups or rings around Saturn, with the first being a background sheet of particles and the subsequent three groups being the inner strand, central core and outer strand, respectively. The central core contained 2×10^6 particles to account for the suspected higher particle densities that are present in the core. The inner strand, outer strand and background population group all contained 1.5×10^6 particles each, distributed randomly with equal probability around the whole ring. The strands and core were all assumed not to be spiral in nature for the sake of our modelling where the true trajectories of particles within these strands can be difficult to model. These distributions are associated with the initial conditions of the particles used in our numerical modelling. They automatically give rise to higher particle number densities in the inner and outer strand and higher again in the central core. This choice has been based on the observations made by *CASSINI*, which have suggested a higher density in a central core and strands (assuming a higher surface brightness).

However, when considering the initial conditions for our numerical model, due to the likely chaotic and non-uniform distribution of clumps or moonlets located in the core (Attree et al. 2013), we neglected their presence. It should then be important to note that most of the mass in the central core and the whole F ring is thought to be confined in the large population of moonlets in the core, which we have omitted from our simulations (Scharringhausen & Nicholson 2013). The existence of these objects in the core would certainly have an effect on the local density changes during an encounter of Prometheus, but it is also probable that some of these same objects are the consequence of such encounters. Therefore, by studying the relative changes in density as Prometheus disrupts the F ring, we hope to further understand the origin of the randomly distributed moonlets. A reference frame has been chosen with Saturn placed at the origin of our system of coordinates, where its initial conditions are associated with a zero-magnitude velocity vector. Therefore, the equations for initial positions of all particles can be shown as

$$\boldsymbol{R}_s = [0, \quad 0, \quad 0] \tag{8}$$

$$\boldsymbol{R}_p = [139,671\ \text{km}, \quad 0, \quad 0] \tag{9}$$

$$\boldsymbol{R}_j = [r * \cos\theta, \quad r * \sin\theta, \quad 0], \tag{10}$$

where r represents the radial position of ring particles from Saturn and θ the angular position of ring particles around Saturn. All ring particles are assumed to have circular-like trajectories located within the F ring; this has been done to help with creating comparable figures that have multiple stages of evolution with respect to orbital periods since the beginning of the numerical model. The initial positions for the radial distances of particles from Saturn are split into four groups or rings to represent the background sheet of particles, inner strand, central core and outer strand, respectively:

$$r(0{:}\ 1, 499, 998) = r_1 + w_1 * \text{random}(n_1), \tag{11}$$

$$r(1, 499, 999{:}\ 3, 499, 998)) = r_2 + w_2 * \text{random}(n_2), \tag{12}$$

$$r(3, 499, 999{:}\ 4, 499, 998)) = r_3 + w_3 * \text{random}(n_1), \tag{13}$$

$$r(4, 499, 998{:}\ 6, 499, 999)) = r_4 + w_4 * \text{random}(n_1), \tag{14}$$

where the number inside the brackets represents the particle ID belonging to each of the four groups. The values r_1, r_2, r_3 and r_4 are the radial distances from Saturn to the inner ring boundary for each of the four ring groups, w_1, w_2, w_3 and w_4 are the widths of each ring and the function 'random(n)' represents a random number generated from 0.000 to 0.999 n_1 or n_2 times.

Each ring inner boundary and width can be shown as

$$r_1 = 139,876\ \text{km} \quad w_1 = 700\ \text{km}$$
$$r_2 = 140,049\ \text{km} \quad w_2 = 70\ \text{km}$$
$$r_3 = 140,214\ \text{km} \quad w_3 = 20\ \text{km}$$
$$r_4 = 140,299\ \text{km} \quad w_4 = 300\ \text{km}.$$

An angular position θ for each of all ring articles has been taken as

$$\theta = 2\pi * \text{random}(N - 2). \tag{15}$$

Velocities of all particles in the initial conditions of our numerical modelling have been derived from equations for circular orbits and given by the following equations:

$$\boldsymbol{R}_s = [0, \quad 0, \quad 0] \tag{16}$$

$$\boldsymbol{R}_p = [0, \quad \nu_p, \quad 0] \tag{17}$$

$$\boldsymbol{R}_j = [\nu * \cos\theta_\nu, \quad \nu * \sin\theta_\nu, \quad 0], \tag{18}$$

where

$$\nu_p = \sqrt{\frac{(G(M_s + M_p))(1 + e)}{(1 - e) * \alpha}} \tag{19}$$

and Prometheus is assumed to be starting at the periapsis of its orbit. This condition is assumed to be the case throughout the manuscript; the parameters of its orbital are taken from Spitale et al. (2006).

The magnitude and angle of the initial velocity vectors of all ring particles can be expressed through the generated random numbers (see equations 8–12) with the use of the formulae:

$$\nu = \sqrt{\frac{G(M_s + M_j)}{r}} \tag{20}$$

$$\theta_\nu = \theta + \frac{\pi}{2}. \tag{21}$$

2.2 Density analysis

All rendered density plots were created using original snapshot files output from our numerical code and used a fake smoothing length assigned to each particle to create an artificial particle density which could be represented relative to all other particles in the ring. This was then used to visualize the relative number density of particles in our figures using SPLASH (Price 2007) a tool for the visualization of smoothed particle hydrodynamics numerical simulations. Only ring particles with the same mass were used in the creation of density plots, i.e. only ring particles. Additional programs were also written in IDL and were used to calculate the max. no. density and the average density of particles within the box at specific points in space and time arising at the evolution of the F ring. Here, unlike previously where a 1000×1000 km box was placed around channel edges

(Sutton & Kusmartsev 2013), we selected the clumps or areas of highest local density and placed a 200 × 200 km box around them. By placing a smaller box around the area of interest, the particle's number density was measured along with the number of particles in the clump, producing a detailed analysis of evolution of density in the clumps. The results obtained with the use of the two models have then been compared in this manuscript.

2.3 Rendered velocity dispersion plots

To further investigate the nature of turbulence in the F ring attributed to Prometheus encounters, additional analysis was done of the outputted data files. Here, particle's velocity magnitude had its unperturbed counterpart removed from its actual value. The resultant magnitude is used to create a rendered plot that shows the spatial distribution of changes in particle's velocity magnitudes. With this approach a spatial investigation into the velocity dispersion and density enhancement can be accomplished.

3 SIMULATION RESULTS

We ran two simultaneous models with and without ring mass (non-interacting and interacting, respectively) and analysed in greater detail the density enhancements previously reported (Beurle et al. 2010; Sutton & Kusmartsev 2013) at the channel edges caused by the interactions of Prometheus on the F ring. Tables 1 and 2 show the max. no. density and average particle density for each clump or where there was an extended area of density enhancement centred over the maximum density.

3.1 Model comparison with the real F ring

In our simulations, the total mass of the F ring modelled is $4.075 \times 10^{-10} M_p$. This is much less than the predicted mass of the clumps in the F ring. If clumps are considered in the central core, their inhomogeneous distribution in the initial conditions makes investigating density variations after the Prometheus encounter become difficult to model. Therefore, we have chosen to neglect the randomly distributed moonlets known to exist in the central core which make up the majority of the mass in the F ring. Instead, we are focusing on the asymmetry first produced during the initial encounter. Surface densities are then 0.000 68 kg m^2, 0.0068 kg m^2, 0.032 kg m^2 and 0.0159 kg m^2 for the background sheet of particles, inner strand, central core and outer strand, respectively. These are much lower surface densities than those used and assumed for the main rings. There it is assumed that the dusty F, G and H rings have considerably lower surface densities than the A, B and C rings system. The number of particles in each of the components is what then affects the surface density of individual strands/core. Also recent developments into the physical properties of the dusty F ring show particles sizes to be considerably smaller than the major Saturnian rings, ∼0.5 μm (Scharringhausen & Nicholson 2013), compared with characteristic particle size distribution in the A and B rings of 30 cm $\alpha_{\min}$ to 20 m $\alpha_{\max}$ (French & Nicholson 2000). Discounting the mass of the moonlets located in the central core, the mass of the remaining F ring is almost negligible (Scharringhausen & Nicholson 2013).

Table 1. The max. no. density of particles and the average particle density within the clumps identified at the channel edge facing away from Prometheus are shown for both the interacting and non-interacting models.

Orbital period (T)	Non-interacting		Interacting	
	Max. no. density	Average particle density	Max. no. density	Average particle density
0	13	5.47	13	5.47
1.5	27	8.61	32	9.41
2.5	17	6.30	19	6.34
3.5	26	8.72	22	8.63
4.5	21	8.11	27	8.85
5.5	26	10.15	26	8.59
6.5	27	10.16	29	10.35
7.5	23	8.95	26	10.14
8.5	30	9.80	31	10.09
9.5	27	9.22	29	9.93
10.5	27	9.45	26	10.05

Table 2. The max. no. density of particles and the average particle density within the clumps identified at the edge facing towards Prometheus are shown for both the interacting and non-interacting models.

Orbital period (T)	Non-interacting		Interacting	
	Max. no. density	Average particle density	Max. no. density	Average particle density
0	13	5.47	13	5.47
1.5	20	7.22	15	5.66
2.5	16	6.30	19	6.05
3.5	23	7.51	22	7.74
4.5	25	8.44	24	8.61
5.5	27	8.21	23	8.35
6.5	24	8.69	29	11.48
7.5	28	9.41	25	9.17
8.5	23	9.20	37	10.75
9.5	26	8.57	29	9.18
10.5	27	10.54	28	10.14

Our model also assumes a monolayer where in reality the F ring and other rings have some vertical component, which also effectively defines the optical depth and subsequent surface density. The F ring actually has the largest vertical component to it, equivalent depth of 10 ± 4 km (Scharringhausen & Nicholson 2013) compared with at least an order of magnitude smaller for the main rings. It should be natural then to assume that future numerical studies of the F ring should include a multilayer/stratified structure, as the vertical component to particles dispersions should play an important role in the chaotic and turbulent environment of the F ring.

Due to resolution limitations in images taken by *CASSINI*, comparable quantitative data of the change in density were difficult to obtain. However, it can be easily seen that there is a clear asymmetry in structures formed by Prometheus noticed in both our simulations and the real F ring, Fig. 2. There is a high discrepancy between the model results and the real F ring (Table 3). It arises on the channel edge facing away from Prometheus at this moment of time. It is because areas of enhanced density on this channel edge obtained in our model are highly localized. It is likely that the resolution in *CASSINI* images effectively smooths out highly localized density increases. On the other hand, in our simulations, we have significantly higher capabilities to resolve genuine maximum increases. In our models, the channel edge that faces Prometheus, (B, D, F) a larger area of enhanced density, is seen; after 5 orbital periods, there arise large chaotic-like fluctuations in the maximum density.

We also note that as the system evolves, density enhancements become more dominant in the central core, residing in the area

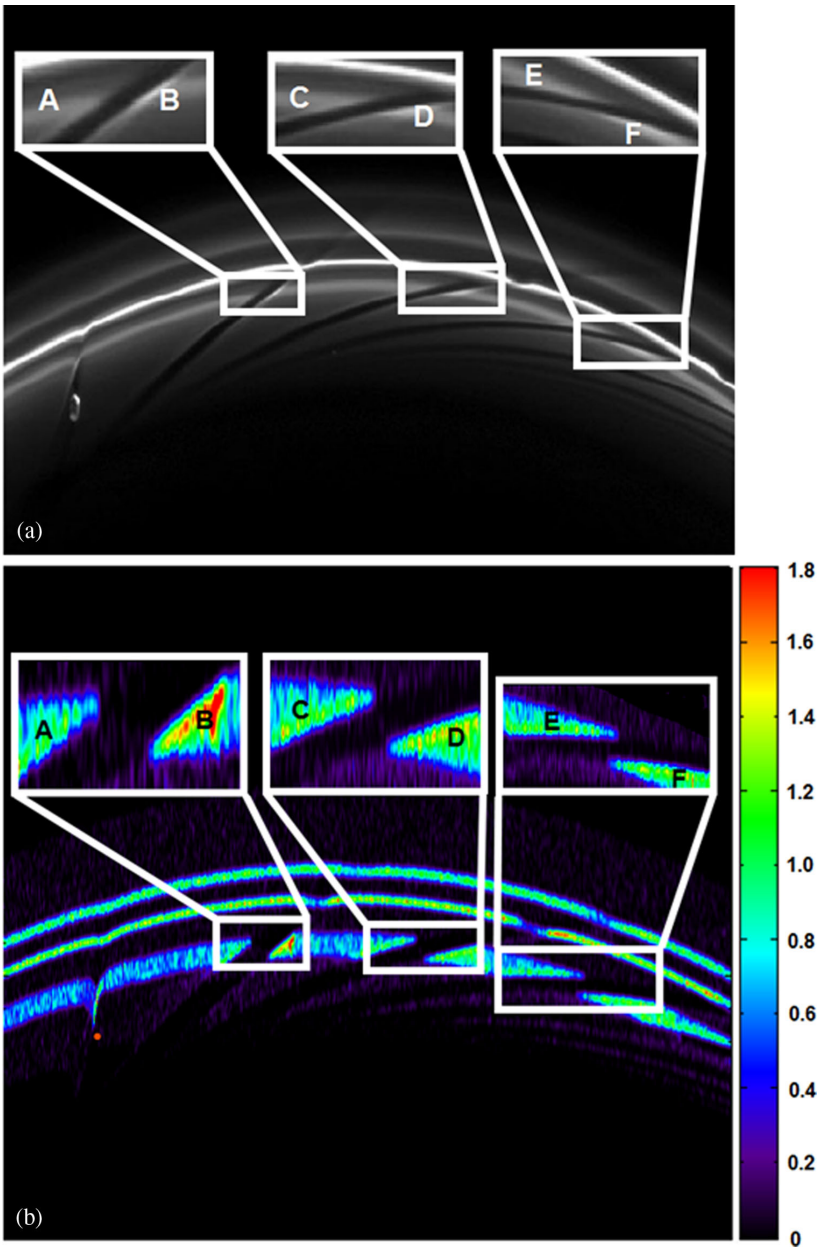

Figure 2. (a) An image taken by *CASSINI* on 2010, June 1 in the narrow angle camera. During the time of the image, *CASSINI* was 808 000 miles from Saturn relating to a 5 miles per pixel resolution. Here, assumptions are made that surface brightness seen in the *CASSINI* images is proportional to surface density (calculated with our model). Surface brightness is normalized to the inner strand. (b) A rendered plot depicting the density calculated with our model at the same orbital phase as seen in the image by *CASSINI*. This density is normalized so that it has a value equal to 1 on the unperturbed inner strand, i.e. the same as in the *CASSINI* image, making density changes in the theory (model) and observations more comparable (Table 3, above). Areas A, C and E represent locations on the channel edge facing away from Prometheus, while areas B, D and F represent locations on the channel edge of the inner strand facing towards Prometheus post-encounter. An orbital phase of 0.57 was assumed to match the observations in our model where the apoapsis of the orbit was at 0.5 and periapsis at 0.0 and 1.0. It is also noted that channels appear at their most open during the apoapsis of Prometheus' orbit, and thus channel edges will show their highest densities at this point.

where a large population of moonlets have been observed (Attree et al. 2012, 2013; Meinke et al. 2012). There is then a clear spatial correlation between surface brightness and surface density which occurs during the evolution of various structures.

3.2 Localized density enhancements

The largest clumps seen at the channel edges were then tracked over multiple orbital periods and compared in Tables 1 and 2. Previously, the channel edges were shown as increasing in density over time, but our results demonstrate that these increases are more localized. This local increase in density within the channel edges is markedly different between the two models, as can be illustrated in Fig. 3.

Fig. 3 illustrates the distinct composition of the localized increase in density witnessed at one of the channel edges 9.5 orbital periods after the initial encounter. What we see is that the non-interacting model shows multiple detached areas of enhanced density whereas the interacting model displays a single well-defined area of

Table 3. The locations (A, . . . ,F) identified in Fig. 2 are listed with their derived change in brightness (*CASSINI*) and density (modelled). Here, for comparison, we have presented the maximum values at these locations.

Region	*CASSINI* (per cent change in surface brightness)	Model (per cent change in particle density)
A	+75 per cent	+83 per cent
B	+10 per cent	+64 per cent
C	+58 per cent	+70 per cent
D	+9.6 per cent	+62 per cent
E	+56 per cent	+60 per cent
F	+9.7 per cent	+58 per cent

increased density. Individual clumps identified in both models do not differ drastically in the max. no. density and average number density. However, it is their shape and ultimate distribution within the channel edge that is in contrast between the models, at 9.5 orbital periods. Although here we only use the channel edge facing away from Prometheus after 9.5 orbital periods, it must be noted that a similar trend was seen at the same channel edge throughout their evolution. This difference between the two models became more apparent as the two models were allowed to evolve over a longer time.

Density profiles of clumps seen in Fig. 3 show that at the channel edge facing away from Prometheus, the average particle number density and the max. no. density for both models is different (Fig. 5b). The interacting model at this point in the evolution of the system exhibits a max. no. density approximately 7.4 per cent higher than the non-interacting model, while the average particle number density is 7.7 per cent higher than the non-interacting model. In the interacting model, a higher proportion of particles with a number density greater than 20 can be seen causing the noticeable difference in average density in the clump. It should be noted here that both models show a similar difference in their maximum and average number densities with very little fluctuations throughout their evolution, thus suggesting a higher degree of stability at this location.

When we consider the same process for the opposite channel edge, it is noted that evolution of the density enhancements does not completely mirror the other edge. Fig. 4 shows the same visual representation of the density distribution within the channel edge facing Prometheus. At these locations, density enhancements for both models are generally over a larger area with an inhomogeneous distribution of clumps within. Here, we see a difference in the most prominent clumps, a difference of 7.1 per cent for the average number density and 11.5 per cent for the max. no. density between the two models, Fig. 5(a).

Overall, the area showing an enhanced density is larger at this channel edge, but when investigated further individual clumps within the enhanced region display increases much greater than the previous edge. This spatial distribution of a larger number of clumps seen over a larger area could account for the reason why we seen an overall higher average surface brightness on the channel edge facing Prometheus in images by *CASSINI*.

Ultimately, these self-gravitating clumps could be dependent on local conditions growing rapidly from one another and might explain why fan structures and moonlets are witnessed predominantly at this channel edge. Additionally, the most striking feature witnessed at this channel edge is that the fluctuations in maximum and average density of clumps in the interacting model are chaotic. Here, the local density is capable of drastic increases over just a few hours, but also the same is true for the rapid dispersion of clumps, thus suggesting a more unstable environment than the opposing channel edge.

Fig. 6 shows the evolution of a channel from 2.5 to 8.5 orbital periods of the interacting model. The most notable thing is the change in locations of highest densities and growth of density, predominantly on the top channel edge (facing Prometheus). This same edge facing Prometheus shows a drifting of the area displaying a density enhancement along with the overall increase in the area. When we consider the density in the largest of the clumps seen at these channel edges, Figs 7 and 8, we see that both channel edges have shown a substantial increase in their average and maximum densities. However, at 8.5 orbital periods, the clump seen at channel edge facing Prometheus (Fig. 8a) shows a large spike in density compared with the non-interacting model at the same time on the opposing channel edge (Fig. 8 b). The exact location of this clump and dramatic local increase is circled in Fig. 6(b), it should be noted that even the rendering of our model is not able to visualize the extent of this localized increase. This sudden increase in density obtained with the interacting model is short lived, decreasing sharply after another orbital period, Fig. 5(a). The nature of the chaotic

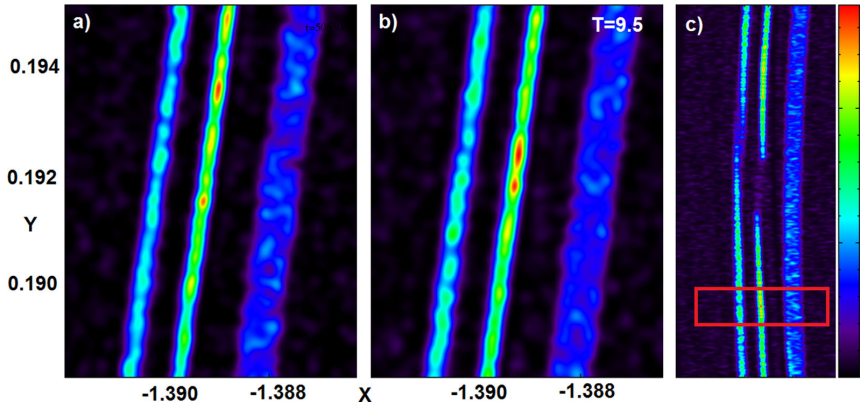

Figure 3. A comparison between the two models is shown at a time of $T = 9.5$, where T is given in Prometheus orbital periods since the start of the simulation, and (a) is for the non-interacting model, (b) for the interacting model and (c) is for a visual representation using the interacting model to show the position on the channel where the snapshots (a) and (b) are taken from. Here, the reference frame is zoomed in to show the clump with the highest density on the channel edge facing away from Prometheus, while the non-interacting model shows a larger single clump associated with much more coherent and defined area of increased density. Although the average density and max. no. density for both areas is only slightly higher for the interacting model it does clearly show a well-defined and larger area than that obtained in the framework of the non-interacting model.

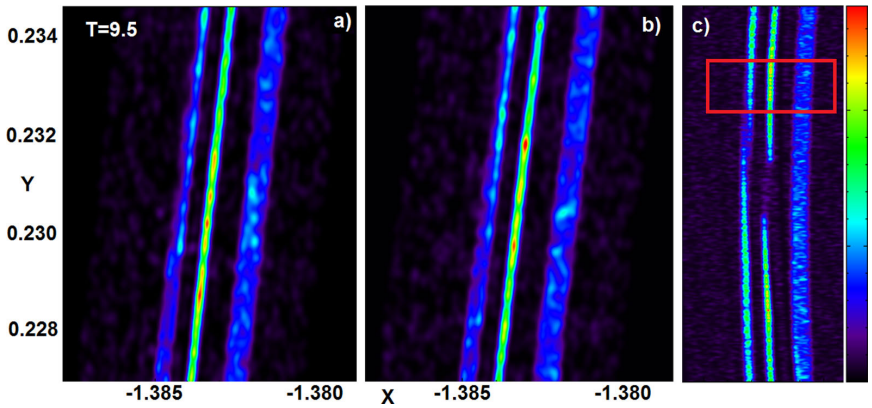

Figure 4. A comparison between the two models is shown at a time of $T = 9.5$, where T is given in Prometheus orbital periods since the start of the simulation and (a) is the non-interacting model, (b) is the interacting model (c) is a visual representation using the interacting model to show the position on the channel that the snapshots (a) and (b) were taken from. Here, the reference frame is zoomed in to show where the clump with the highest density is chosen on the channel edge facing Prometheus. The most notable thing here is that unlike in Fig. 3, the structure of the opposite channel edge in the framework of the interacting model does not show a single coherent area of enhanced density. Instead, like in the non-interacting model, the local regions of enhanced density are sprawled here over a larger area with multiple clumps.

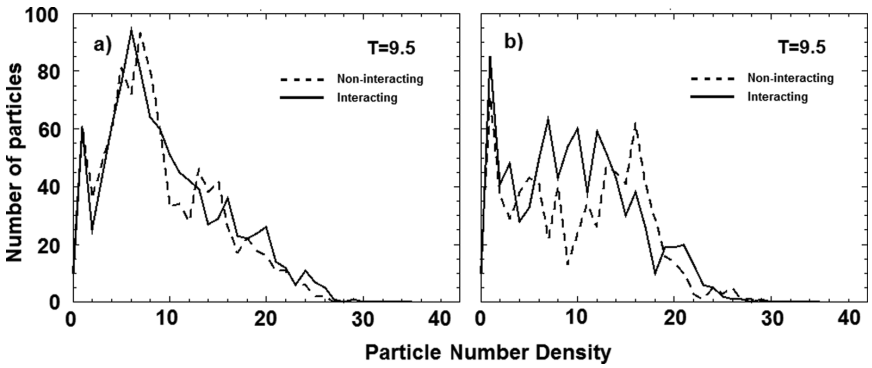

Figure 5. Comparison of density profiles for both the non-interacting and interacting models centred on the most prominent clump where (a) is the channel edge facing Prometheus (Fig. 3) and (b) is the channel edge facing away from Prometheus (Fig. 4). T is the time given in Prometheus orbital periods. The density profiles here are for the most prominent clumps shown in Figs 3 and 4. The profiles of the density distribution in both clumps show that max. no. density does differ from each model, with the most notable being the channel edge facing away from Prometheus (b).

fluctuations can easily be seen when comparing the density profiles seen Figs 5(a) and 8(a). The overall area where clumps are distributed on the opposing channel edge, bottom Fig. 6, does not increase drastically in the same way as the above channel. Moreover, there does not appear to be any particle drift as a result of elastic collisions. Here, we would expect a diffusion of particles from high-density regions to lower density high-density areas. From results obtained from our model, Fig. 6, we can conclude that low-density regions at 2.5 orbital periods continue to decrease while high-density regions increase, and in some cases quite dramatically. The low particle density in our model, 0.17 per km^2, means that very few collisions would actually take place anyway.

3.3 Accelerated growth

Additional analysis of the results obtained with our numerical models was done in the form of mapping, in high resolution, velocity dispersion during an encounter of Prometheus with the F ring. Here, two-dimensional rendered plots were created to spatially resolve the variations in the velocity magnitude of ring particles from their initial unperturbed velocity, referred to as v_d velocity dispersion:

$$v_d(t_1 - t_2, x, y, z) = |\boldsymbol{v}(t_1, x, y, z) - \boldsymbol{v}_{up}(t_2, x, y, z)|, \quad (22)$$

where t_1 and t_2 represent a time pre- and post-encounter of Prometheus on the ring, respectively, and v_d, $\boldsymbol{v}$ and $\boldsymbol{v}_{up}$ is the magnitude of the velocity dispersion, the velocity post-Prometheus encounter and the unperturbed velocity, respectively, at any given time. Maps were created for the results of both models in the same way that density maps were created in the sense that all particles have a calculated quantity assigned to it, which can then be two-dimensionally rendered. Although here a different colour scheme scale was used to show dispersion values higher (red) and lower (blue), with the unperturbed ring particles set at zero (green). Creating maps like these allowed us to form a link between maximum and minimum velocity dispersions and their locations within the streamer-channel structures. What we find is that a quick glance shows there to be little difference between the results of the two models. However, when certain features are zoomed into, it starts to become clear that the localized density variations correspond to the same difference and local variations in velocity dispersion. Fig. 9 compares the results of the two models at time $T = 6.91$(Prometheus orbital periods) after the start of the simulation. Here, we can see that areas of the first two channels (top zoomed into section, Figs 9a and b) show a complete opposite distribution to one another internally. Maximum velocity dispersion calculated in both models at this location is at opposite ends of the feature. The zoomed

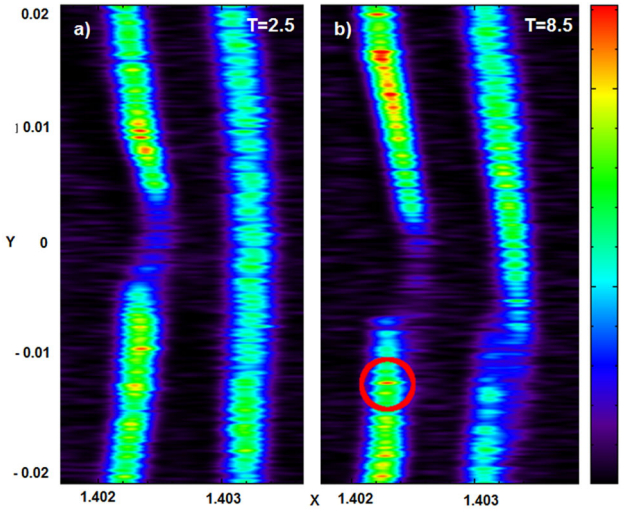

Figure 6. Shown here are the density maps of two channels in the central core (left) obtained from our results, differing in evolution from (a) 2.5 orbital periods and (b) 8.5 orbital periods from start of simulation for the interacting model only. Both channels are rotated about the origin so that they are centred on the *Y*-axis at zero. The clump circled in (b) on the bottom channel edge shows considerably higher maximum and average densities than the oppose channel edge and the non-interacting model, see Fig. 8a.

areas at this time period represent the centre of the channel when Prometheus is at periapsis and where particles rush back in to fill the gap. However, when we consider the two models, there is an asymmetry in the locations of maximum dispersion; the non-interacting model (Fig. 9a) shows the highest towards the channel edge facing away (top of zoomed section), while the interacting model displays the most extreme near the edge facing towards Prometheus (bottom of zoomed sections). Another intriguing difference between the two models is that in the framework of the non-interacting model, multiple locations of maximum dispersion are observed chaotically positioned within the channel. In contrast, the interacting model at the same time period always shows one quite defined area on one channel edge facing towards Prometheus. Density maps of the same area have revealed that there is an asymmetry between the distributions on the channel edges. Again, we see a similar asymmetry for the velocity dispersion maps and that this could be an underlying clue to this mystery.

As previously suspected, channel edges facing Prometheus saw local density distributions to be scattered over a larger area with larger fluctuations for the interacting model than the non-interacting model. The possible culprit of this was suggested to be additional turbulence in the movement of particles at this location. The non-interacting model repeatedly produces a more chaotic distribution of particles exhibiting the maximum dispersion consistent with the more dispersed distribution of localized density enhancements on both channel edges.

If the numerical simulations are allowed to evolve further, say another two orbital periods, we see deterioration in the asymmetry in the local distribution of velocity dispersion between the models (Fig. 10). Although there does still exist some asymmetry between the areas showing the maximum values, it has somewhat diminished. The interacting model still shows a bias towards the channel edge facing Prometheus and the non-interacting model on the edge facing away.

However, it is the area around the centre of the channel that now shows the divergence between the results obtained with the

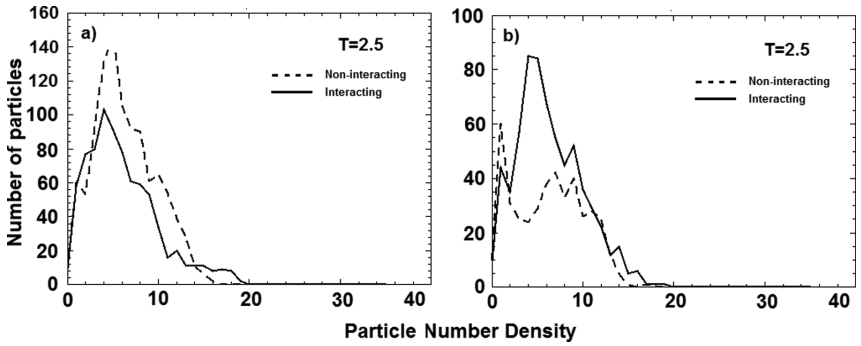

Figure 7. Comparison of density profiles at the channel edges obtained with the non-interacting and interacting models where (a) is the channel edge facing Prometheus and (b) is the channel edge facing away, and *T* is in Prometheus orbital periods.

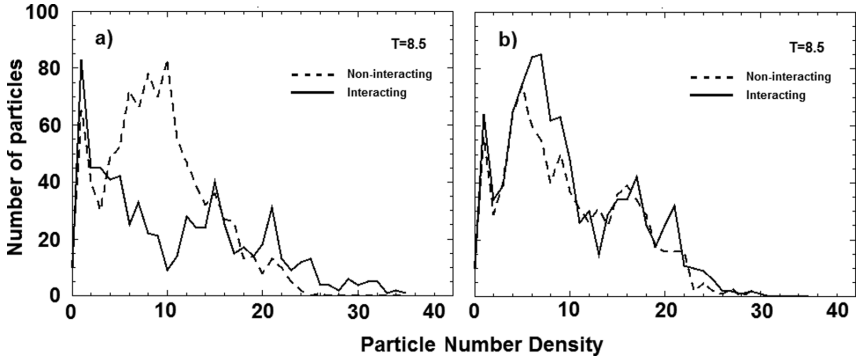

Figure 8. Comparison of density profiles at the channel edges obtained with the non-interacting and interacting models where (a) is the channel edge facing Prometheus and (b) is the channel edge facing away, and *T* is in Prometheus orbital periods.

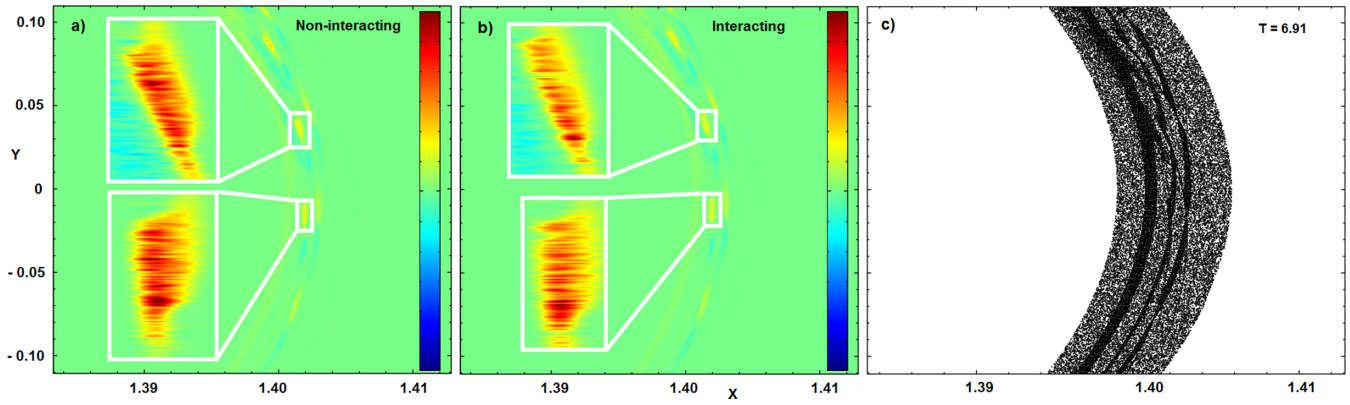

Figure 9. Velocity dispersion maps are shown for both the (a) non-interacting model and (b) interacting model at a time of $T = 6.91$, where T is given in Prometheus orbital periods and (c) shows the positions of particles at the same time. Both the X and Y-axes scales are in 2×10^5 km. The zoomed in section is rescaled to represent the positions of the maximum localized velocity dispersion.

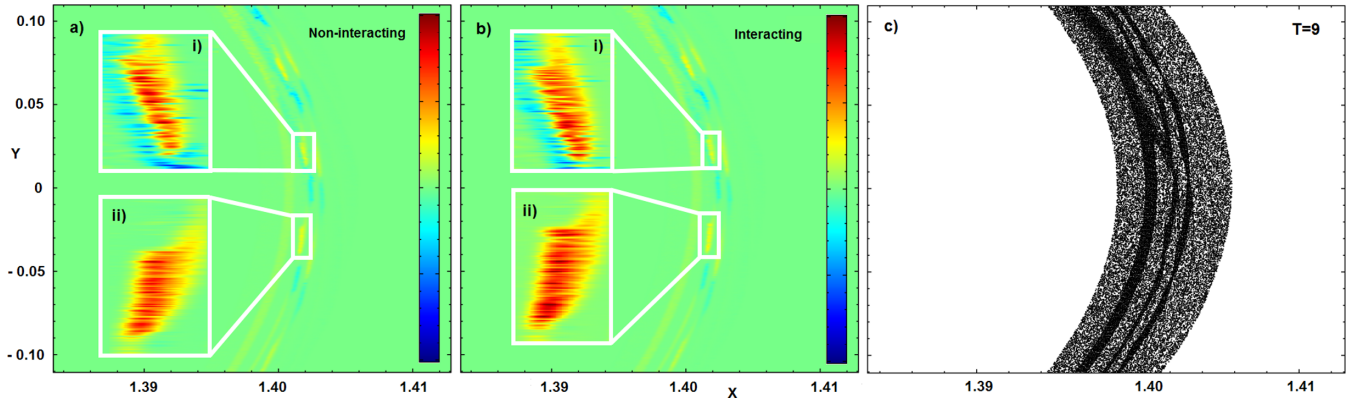

Figure 10. Velocity dispersion maps are shown, obtained in the framework of both the (a) non-interacting model and (b) interacting model, and (c) shows the positions of particles at a time of $T = 9$, where T is given in Prometheus orbital periods. Both the X- and Y-axes scales are in 2×10^5 km. The zoomed in section is rescaled to represent the positions of the maximum localized velocity dispersion, where (i) and (ii) are the centre of the channel's position when Prometheus is at periapsis of its orbit, 7.5 and 8.5 orbital periods after the initial encounter, respectively.

two models. Here, on the channel edge after 7.5 orbital periods of the initial encounter (Fig. 10a-i) there are individual particles that show negative velocity dispersion amongst the area that has overall increased velocity dispersion. This shows the main differences associated with the gravitational interactions taken into account in one of the models. Particles that move on their own trajectories are free to evolve through Keplerian shear with no additional forces outside those of Saturn and Prometheus; it is these particles that are starting to bleed into the streamer-channel structures creating an inhomogeneous distribution of velocity dispersion.

If we now look at the younger structures created by the encounter, 0.5 orbital phases different than those presented in Figs 9 and 10, there appear to be little differences between the results of the two models. The most notable difference is shown in Fig. 11 where the channels are at an orbital phase corresponding to when the channels are close to their most open position. Here, on the channel created after two orbital periods from the initial Prometheus encounter (zoomed section, Fig. 11), we see a difference only in the particles displaying an increase in their velocity magnitude compared (orange) with the normal Keplerian velocity. The distribution of particles with a lower velocity shows no difference between the two models close to the encounter. What we find is that the non-interacting model provides a more dispersed velocity distribution and a much larger spike in the local velocity than the interacting model for the same chosen area. We obtain that these younger areas in the channels (inner strand) quickly become less important to the evolution of the system and the ultimate distribution of localized density enhancements because Keplerian shear promptly distorts and mixes particles in this area.

To further investigate the idea of a spatial link between maximum densities and velocity dispersions, direct comparisons were made in Fig. 12. Here, we have identified the locations of maximum density and dispersion and found generally that there is a spatial link between the highest density and the highest dispersions obtained with the interacting model. In contrast, the non-interacting model does not explicitly show the same link with a disparity in the locations of maximum density and dispersion.

4 DISCUSSION

A spatial investigation of density enhancements in Prometheus-induced structures leads to the conclusion that asymmetry between the two channel edges matches the same asymmetry in the real F ring. Here, previous images taken by *CASSINI* (Fig. 13; Beurle et al. 2010) appear to show fan structures predominately on the channel edges facing towards Prometheus. Many of the fans also show a linear growth proportional to orbital period after initial encounter. In our models, we see on the same channel edge the greatest sudden increases in local density after 5 orbital periods in the interacting model. Where density increases beyond the Roche

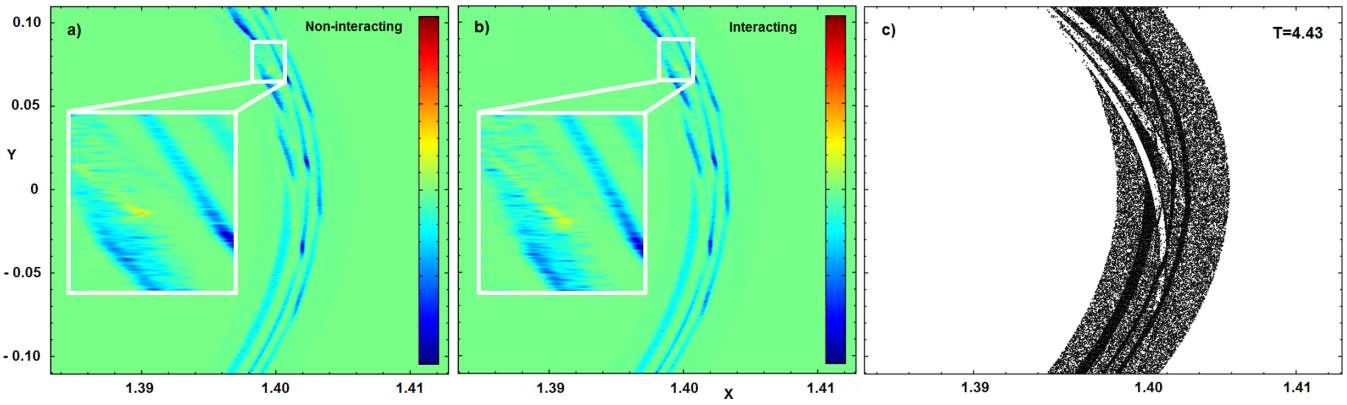

Figure 11. Here, we show velocity dispersion maps obtained with the (a) non-interacting model and (b) interacting model at a time of $T = 4.43$, where T is given in Prometheus orbital periods, and (c) shows the positions of particles at the same time. Both the X- and Y-axes scales are in 2×10^5 km. The zoomed in sections show areas obtained with the two models that display differences in the distribution in the local velocity dispersion, at the time when the channels are near to their most open position. The zoomed in section showing the difference between the results of the two models is on a channel created two orbital periods after initial encounter towards the edge facing Prometheus.

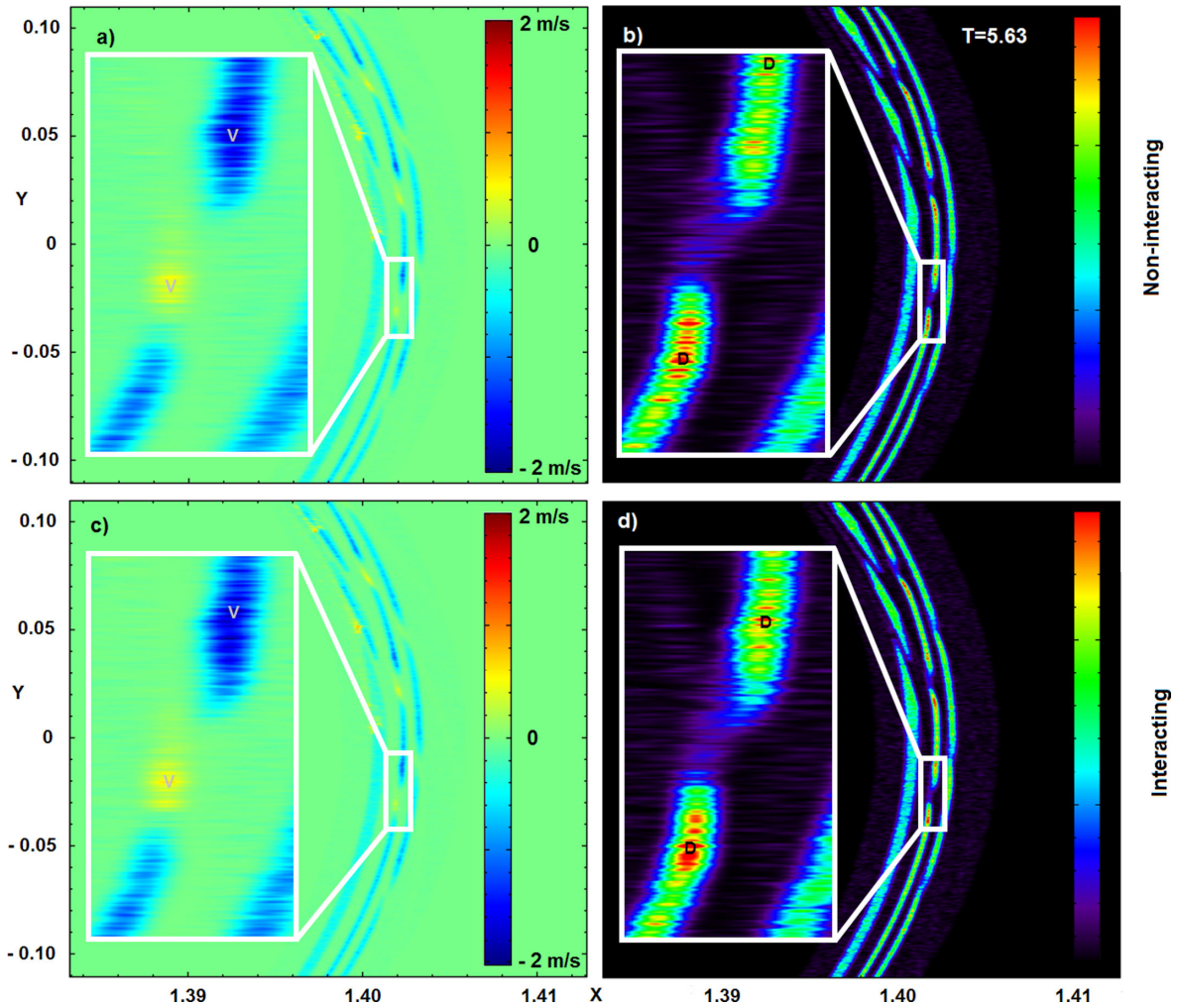

Figure 12. Velocity dispersion and density maps are shown for both the (a), (b) non-interacting model and (c), (d) interacting model at a time of $T = 5.63$, where T is given in Prometheus orbital periods and Both the X- and Y-axes scales are in 2×10^5 km. The zoomed in sections represent a complete channel showing the asymmetry in velocity dispersion and density between the opposing edges. The locations of the maximum and minimum values for the velocity dispersion and number density are indicated in each zoomed section as V or D, respectively. The linear scales used to display both the velocity dispersion and the density in the zoomed sections are rescaled to show the distribution of the maximum values; however, both zoomed areas use the same scale and are therefore comparable.

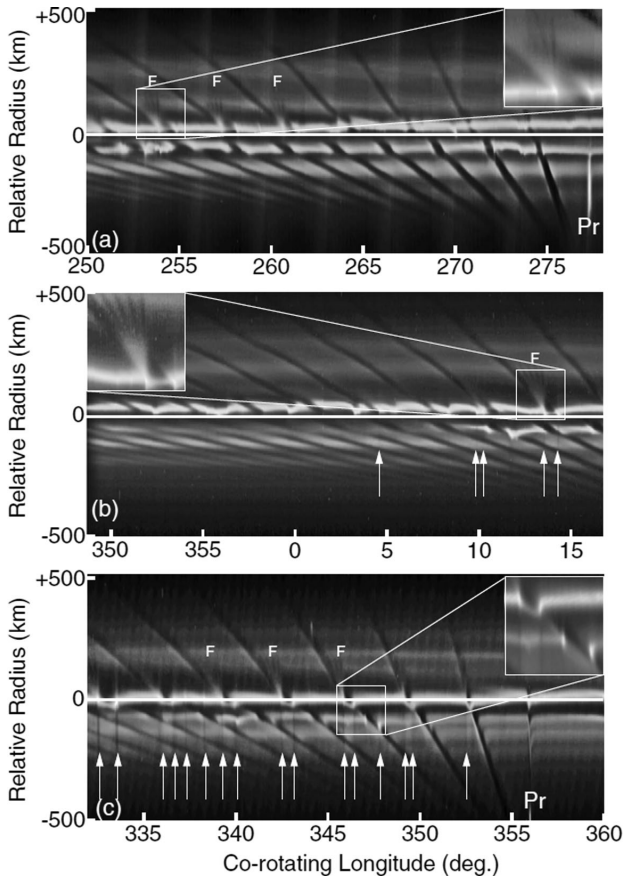

Figure 13. Taken from Beurle et al. (2010), the figure shows three 28° sections of the F ring created by mosaics of multiple images where the *x*-axis represents a corotating longitude system and the *y*-axis as a relative radial position from Saturn. In all frames, 'F' indicates the longitudinal position of an embedded object in the central core and where appropriate 'Pr' denotes the position of Prometheus. Dates of image capture are (a) 2008 July 5, (b) 2008 December 8 and (c) 2009 April 16.

density for F ring, clumps could become coherent objects capable of forming fans over many subsequent orbits. The spatial agreement in our models and the real F ring suggest that the large fluctuations seen at this channel edge could be responsible for the embedded objects that create the fans on this particular channel edge. Or if not solely the outcome of a single encounter on a homogeneously distributed core, as we have modelled, the density increases on an already chaotically distributed core by Prometheus would lead to the collapse of clumps on a random selection of channel edges. Again a random distribution of fans is seen on channel edges with many not showing any evidence of embedded moonlets.

A surprising outcome from our simulations was the discovery of a spatial link to the highest velocity dispersions and the highest density enhancements, found only in the framework of the interacting model. General consensus surrounding velocity dispersion and max. no. densities of particles is that high velocity dispersions lead to the lowering of the local density, amounting to a fragmentation of the area, and has been shown to be consistent across many different models of Saturn's rings (Beurle et al. 2010; Esposito et al. 2012; Torres, Madhusudhanan & Esposito 2013). In our simulations, the highest velocity dispersions and densities occur at the same time and location. However, this result could also give light to the reason why we see large chaotic fluctuations in density at the channel edge facing Prometheus. The high velocity dispersions, located on one channel edge, give rise to a more turbulent and unstable environment that the clumps reside in. However, it also could in some cases help in the rapid collapse to form coherent objects or moonlets and the apparent random positioning of fans on some channel edges.

4.1 Considerations when employing our models

If we consider that the viscosity component may originate from the collisions and gravitational interaction between particles, we can make some assumptions and estimate the magnitude and value of the likely viscosity present. The collision rate between particles will be an important factor influencing the outcome of the viscosity magnitude. In our simulations, we have an initial maximum average particle density of 0.17 particles per km^2. Low particle densities such as these are unlikely to experience any significant rate of collisions, especially when collision rates are proportional to the distance that separates the particles. Even when physical particle sizes are considered due to the small particle density, the collision rates are unlikely to rise to anything significant. Thus, for the results obtained with our models, physical collisions between particles have negligible effect on the overall evolution of the system, regardless of the collisionless/collisional dynamics employed. Unlike other modelling that investigated the effect of larger stationary moonlets in the A ring (Lewis & Stewart 2009), with which the particles would collide, we are only concerned with gravitational interactions between ring particles. Here, Prometheus is assumed to have very little physical collisions with F ring particles, instead the evolution of the system is dominated by the effect of gravitational scattering. The smaller particle sizes known to exist in the F ring (Scharringhausen & Nicholson 2013) also mean that the magnitude of any likely viscosity resulting from collisions would be much smaller than witnessed in Saturn's main rings.

As particle number density is proportional to collision rates, where particle sizes remain the same, a high density relates to a high viscosity and a low density to a lower viscosity. Fluids comprised of particles with larger radius will consequently expect to have higher collisional rates than fluids with the same number density but with particles of a smaller radius. If we do assume particles to have a physical size, collisions will occur when the particles are moving towards each other as well as when the shortest distance between them on their trajectories will be less than the sum of their radii. To make this assumption, all particles should be treated as solid spheres and of the same radius. For collisions to happen, the smallest separation between them will be 2α, where α is the radius of a particle. Therefore, the collisional cross-section can be shown as $A = 4\alpha^2$. From this, we can see that the area where collisions can occur increases as a square with increasing particle radius α. The probability of a collision will increase proportional to the cross sectional area so that the probability $\propto\alpha^2$. With particles that are very small and treated as point masses (as is the case with in our models), the chance of collisions is very small, while the collisional probability for much larger particles is considerably larger. It seems that this collisional component of viscosity is unlikely to contribute anything of significance to the evolution of our system.

The other factor, which is a stronger contribution effecting viscosity, is the gravitational attractive forces between particles. Here, like for all other astrophysical discs, we have a shearing flow as a function of r, which is the radius from the orbital centre (Saturn) of the system. A velocity gradient exists between Keplerian shearing flow layers as function of r, where the velocity of the layer is

proportional to $\sqrt{r}$. When two layers are located at r_1 and r_2, the difference in the Keplerian flow can be given as

$$v_s = \sqrt{\frac{\mu}{r_1}} - \sqrt{\frac{\mu}{r_2}}. \quad (23)$$

Here, we assume circular orbits. The total force exerted by one layer on to another assuming fluid mechanics of a gas can be shown as

$$F = k(2\pi r_1, z) \cdot \left(\frac{\left(\sqrt{\frac{\mu}{r_1}} - \sqrt{\frac{\mu}{r_2}}\right)}{(r_1 - r_2)} \right), \quad (24)$$

where r_1 and r_2 are the radial locations of these two layers, z is the vertical height of the disc, $(r_2 - r_2)$ is the separation between the layers and $(2\pi r_1 \cdot z)$ is the area under consideration.

The viscous shear stress can be expressed as

$$\tau = \frac{F}{A} = k \left(\frac{\left(\sqrt{\frac{\mu}{r_1}} - \sqrt{\frac{\mu}{r_2}}\right)}{(r_1 - r_2)} \right). \quad (25)$$

After simple calculations, considering thinner layers, it is further reduced to $\tau = k \left(\frac{\sqrt{\mu^{1/2}}}{R^{3/2}} \right)$, where R is the radial distance to the layer under consideration.

From equation (24), it is clear to see that the vertical height, z, of the astrophysical disc in question plays an important role in the magnitude of the viscosity. Our models only assume a monolayer of particles which again reduces the overall force exerted on each layer.

Another element that was ignored and deemed to have a negligible effect on the evolution of the system for the time-scales being observed was the mutual precession between the ring particles and Prometheus' orbits. At $0.^{\circ}057\ d^{-1}$, the precession between the orbits and their alignment varies very little when only considering a few orbital periods (Chavez 2009).

Although it is true that a more complete system of Saturn's moons will have an effect on vortex formation in any of the rings, we believe that this will have a negligible effect on the very short term effects of localized disruption during an encounter. Since we are initially looking, in this manuscript, to investigate density asymmetry created during the encounter with Prometheus and not the long-term effects built up with resonances over time, we feel this is a fair assumption to make. It is likely that the most significant effects of additional moons will be seen when Prometheus or the disrupted F ring material is in a radial alignment with Saturn and the additional moons. As a result, it is likely that during the time interval of our simulations this would not be seen. However, this question does pose some interest to our models. Modelling the extended satellite system of Saturn in additional to our current simulations would prove to further clarify any impact of external moons on the evolution of F ring particles.

ACKNOWLEDGEMENTS

This research has made use of data obtained by the *CASSINI* project from the Planetary Data System (PDS).

AUTHOR CONTRIBUTIONS

PJS performed the numerical simulations, analysed the results and wrote the manuscript. FVK contributed ideas, took part in discussions of results and helped with editing of the manuscript.

COMPETING FINANCIAL INTERESTS

The authors declare no competing financial interests.

REFERENCES

Attree N. O., Murray C. D., Cooper N. J., Williams, 2012, ApJ, 755, 27
Attree N. O., Murray C. D., Williams G. A., Cooper N. J., 2013, Icarus, 227, 56
Beurle K., Murray C. D., Williams G. A., Evans M. W., Cooper N. J., Agnor C. B., 2010, ApJ, 718, L176
Boley A. C. et al., 2012, ApJ, 750, L21
Charnoz S., Porco C. C., Déau E., Brahic A., Spitale J. N., Bacques G., Baillie K., 2005, Science, 310, 1300
Charnoz S., Salmon J., Crida A., 2010, Nature, 465, 752
Chavez C. E., 2009, Icarus, 203, 233
Chiang E., Kite E., Kalas P., Graham J. R., Clampin M., 2009, ApJ, 693, 734
Esposito L., Meinke J., Colwell J. E., Nicholson P. D., Hedman M. M., 2008, Icarus, 194, 278
Esposito L. W., Albers N., Meinke B. K., Sremčević M., Madhusudhanan P., Colwell J. E., Jerousek R. G., 2012, Icarus, 217, 103
French R. G., Nicholson P. D., 2000, Icarus, 145, 502
Hedman M. M., Nicholson P. D., Showalter M. R., Brown R. H., Buratti B. J., Clark R. N., Baines K., Sotin C., 2011, Icarus, 215, 695
Kasper M. E. et al., 2008, Proc. SPIE, 7015, 70151S-70151S-12
Lewis M.C., Stewart G. R., 2009, Icarus, 199, 387
Meinke B. K., Esposito L. W., Sremčević M., 2011, EPSC-DPS Joint Meeting, Transient Clumps in Saturn's F Ring. p. 1455
Meinke B. K., Esposito L. W., Albers N., Sremčević M., 2012, Icarus, 218, 545
Murray C. D., Chavez C., Beurle K., Cooper N., Evans M. W., Burns J. A., Porco C. C., 2005, Nature, 437, 1326
Murray C. D., Beurle K., Cooper N. J., Evans M. W., Williams G. A., Charnoz Sé., 2008, Nature, 453, 739
Price D. J., 2007, Publ. Astron. Soc. Aust., 24, 159
Scharringhausen B. R., Nicholson P. D., 2013, Icarus, 226, 1275
Spitale J. N., Jacobson R. A., Porco C. C., Owen W. M., 2006, ApJ, 132, 692
Springel V., 2005, MNRAS, 364, 1105
Srem evi M., Schmidt Jü., Salo H., Seiß M., Spahn F., Albers N., 2007, Nature, 449, 1019
Sutton P. J., Kusmartsev F. V., 2013, Sci. Rep., 3, 1276
Tiscareno M. S., Burns J. A., Hedman M. M., Porco C. C., Weiss J. W., Dones L., Richardson D. C., Murray C. D., 2006, Nature, 440, 648
Tiscareno M. S., Burns J. A., Hedman M. M., Porco C. C., 2008, AJ, 135, 1083
Torres P. J., Madhusudhanan P., Esposito L. W., 2013, Physica D, 259, 55

SUPPORTING INFORMATION

Additional Supporting Information may be found in the online version of this article:

Supplementary Information: Additional density profiles of clumps seen at channel edges are shown where (a) represents the channel edge facing Prometheus and (b) the channel edge facing away from Prometheus. Both the non-interacting and interacting model is shown on the same plot to illustrate the differences between them (http://mnras.oxfordjournals.org/lookup/suppl/doi:10.1093/mnras/stt2462/-/DC1).

Please note: Oxford University Press is not responsible for the content or functionality of any supporting materials supplied by the authors. Any queries (other than missing material) should be directed to the corresponding author for this paper.

This paper has been typeset from a Microsoft Word file prepared by the author.